

Synchronous Chip-to-Chip Communication with a Multi-Chip Resonator Clock Distribution Network

Jonathan Egan, Max Nielsen, Joshua Strong, Vladimir V. Talanov,
Ed Rudman, Brainton Song, Quentin Herr, and Anna Herr
*The authors are with Northrop Grumman Corp., Baltimore, MD 21240**
(Dated: 28 April 2021)

Superconducting digital circuits are a promising approach to build packaged-level integrated systems with high energy-efficiency and computational density. In such systems, performance of the data link between chips mounted on a multi-chip module (MCM) is a critical driver of performance. In this work we report a synchronous data link using Reciprocal Quantum Logic (RQL) enabled by resonant clock distribution on the chip and on the MCM carrier. The simple physical link has only four Josephson junctions and 3 fJ/bit dissipation, including a 300 W/W cooling overhead. The driver produces a signal with 35 GHz analog bandwidth and connects to a single-ended receiver via 20 Ω Nb Passive Transmission Line (PTL). To validate this link, we have designed, fabricated and tested two 32 \times 32 mm² MCMs with eight 5 \times 5 mm² chips connected serially and powered with a meander clock, and with four 10 \times 10 mm² chips powered with a 2 GHz resonant clock. The meander clock MCM validates performance of the data link components, and achieved 5.4 dB AC bias margin with no degradation relative to individual chip test. The resonator MCM validates synchronization between chips, with a measured AC bias margin up to 4.8 dB between two chips. The resonator MCM is capable of powering circuits of 4 million Josephson junctions across the four chips with a projected 10 Gbps serial data rate.

Data movement efficiency drives overall power consumption and performance in large-scale digital systems. Industry trends include optimization of architectures and algorithms to minimize data movement, and the use of energy-efficient optical interconnects on all levels of the system from the chip, to the rack, to the data center [1]. Superconducting digital technology has the unique advantage of lossless, high bandwidth wires—with optical-like properties—but using the native signal levels and the native fabrication process [2]-[5]. This avoids the overhead of low conversion efficiency associated with optical. Superconducting on-chip interconnects can transfer signals with 0.1 fJ/bit total dissipation, including 300 W/W cooling overhead, over distances of 30 mm [6].

Superconducting lossless interconnect also enables integration of chips and chiplets into a multi-chip module (MCM) with low overhead and yield advantages [7]. This approach—long recognized in the context of superconductivity—is now in full alignment with the post-Moore industry trend towards new approaches to mitigate unsustainable demand for computer power and unsustainable hardware production cost. On the architecture side, the rise of domain-specific hardware, heterogeneous systems, and chiplets integration are moving the industry away from general purpose processors and system-on-chip with ever-increasing integration density [8]. On the hardware side, advanced packaging like 3D-IC

enables new data protocols with increased pin and packaging density [9]. All these advancements would be of great effect when applied to superconducting technology due to volumetric cooling. Cryogenic cooling is applied to the entire system instead of to individual chips, enabling extremely high compute density with all components of the superconducting system physically and electrically close. An ExaFlop system might have the physical size of three electronics racks [10].

The superconducting MCM is a primary component of a large scale integrated cryogenic system. It consists of superconducting chips with active logic and memory, mounted on a passive superconducting carrier. Superconducting energy-efficient logic families such as RQL [11] and ERSFQ [12] support direct transfer of ps data pulses on passive transmission line interconnects [13], [14] (AQFP technology requires costly energy conversion to RSFQ [15]). Flip-chip packaging with low resistance bumps [16], [17] means that there is no energy penalty to transfer data off-chip. Total shoreline bandwidth, which is a product of the number of signal lines and the clock rate, is limited only by bump pitch.

Starting from the pioneering demonstration of 60 Gbps chip-to-chip communication [7], there has been steady progress in developing superconducting MCMs [5], [14], [16]-[19] and off-chip communication, including the recent demonstration of a 16-bit bus [14]. Typical demonstrations involve a single chip mounted on the MCM with driver and receiver located on the chip, and passive transmission lines on the superconducting carrier. These demonstrations are important for feasibility study of maximum data transmission [5], [18] and optimization of MCM link [19]. However, single-chip circuits avoid the problem of timing synchronization that is central to larger, real-world systems.

* This research is based upon work supported in part by the ODNI, IARPA, via ARO. The views and conclusions contained herein are those of the authors and should not be interpreted as necessarily representing the official policies or endorsements, either expressed or implied, of the ODNI, IARPA, or the U.S. Government.

With typical clock frequencies for SFQ technologies of 2-60 GHz [13], [20], [21] timing synchronization between chips on MCM is an important aspect of the system design. The local clocking in RSFQ logic families makes it particularly challenging, and would appear to require complicated clock recovery and channel de-skew. The AC-biased circuits of RQL have the important advantage of enabling synchronous communication using a resonant clock network on chip and between chips.

We report the first demonstration of a superconducting multi-chip MCM with synchronous chip-to-chip links. The paper presents design and test cycles 1) of nine $5 \times 5 \text{ mm}^2$ chips on an MCM with a meander clock and characterized vs. clock rate, and 2) extension to four $10 \times 10 \text{ mm}^2$ chips on an MCM with a global resonant clock to demonstrate scalability.

I. CHIP-TO-CHIP SYNCHRONOUS COMMUNICATION IN RQL

RQL technology is the first superconducting digital technology to efficiently use AC power distribution using a resonant network. The on-chip resonant clock and power network, implemented using metamaterials [22], is a proven enabler for scaling to complex digital logic. The network has a Zeroth-Order Resonance (ZOR) mode, providing uniform amplitude and zero clock skew across the chip. Low skew enables synchronous communication. For a multi-chip system the approach is extended to a clock network across chips, with chip-to-chip communication.

The critical innovation that enables synchronous communication on the MCM is a dendritic resonator network implemented on the carrier, which we call a “MegaZOR.” The MegaZOR, designed to the same resonance frequency as the individual chips, performs several functions. A primary function is to equalize phases and amplitudes of the clock signals on the chips. The chips are not isolated, but instead the network causes them to operate as a single resonator while tolerating a spread in their resonant frequencies that may be larger than the individual resonance peaks. This is achieved by a network of multiple passive transmission line segments, optimized for a uniform response in amplitude, frequency and phase of the on-chip resonators. The MegaZOR also transforms the impedance from the 50Ω drive to the small $22 \text{ m}\Omega$ impedance of the on-chip resonators, four of which are driven in parallel.

The synchronous data link across the MCM requires that the chips have the same frequency, phase, and amplitude within tight limits for fabrication process variations. The delay between driver and receiver is determined by signal propagation time on superconducting Passive Transmission Lines (PTL) on the carrier. The clock phase in degrees of the receiver, θ_r , is

$$\theta_r = \theta_d + \tau_{\text{PTL}} \times f_{\text{res}} \times 360^\circ,$$

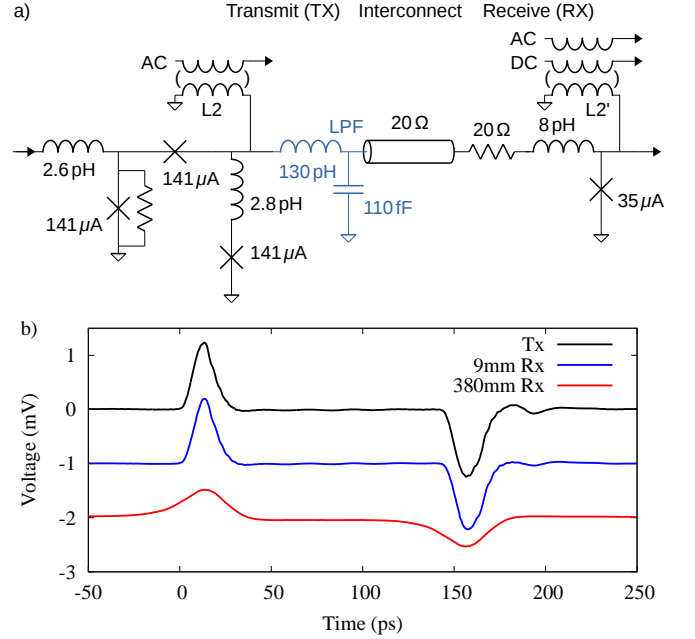


FIG. 1. LBW synchronous communication link. a) The driver low-pass filters several underlying SFQ pulses generated by undamped, latching junctions to produce a Gaussian-pulse with 35 GHz spectral bandwidth. The 20Ω interconnect is terminated at the receiver, which recovers the bipolar RQL-encoded data. b) Spectre-simulated waveforms at the driver output (Tx) and receiver input (Rx) show the attenuation and dispersion of the LBW pulse propagating over 9 mm short and 380 mm long PTLs. For clarity, propagation delay is subtracted from each waveform, and the waveforms are progressively offset by -1 mV .

where θ_d is the phase of the driver, τ_{PTL} is the electrical length of the PTL, and f_{res} is the frequency of the clock. Latency may exceed one clock cycle, so the phase is wrapped, e.g. if the PTL delay were 1025 ps corresponding to a 100 mm length and the phase of the driver were 90° , then $\theta_r = 90 + 1025 \text{ ps} \times 5 \text{ GHz} \times 360^\circ = 1935^\circ$, and subtracting 5×360 would yield the nominal receiver phase of $\theta_r = 135^\circ$. Synthesis and timing analysis tools treat the MCM system as a single chip and assign the phase of each receiver post-layout. Synchronous communication can be used in systems where the fabrication-related skew between wires is small relative to the timing window of the receiver, about one phase of the RQL clock. For larger systems involving board-to-board communication isochronous protocol is required, as described in [23].

An important component for long-range RQL data links is a driver with improved bandwidth efficiency. Our Low Band-Width (LBW) driver has about ten times less analog spectral bandwidth than the single-flux-quantum (SFQ) pulse. Superconducting PTLs have some loss and dispersion at RF frequencies which can degrade the signal over distance. As first described in [24] and experimentally confirmed in [6], a single SFQ pulse with ps-scale

width has a limited range of about 10 mm on typical Nb passive transmission lines of sub-micron width. Increasing the pulse width increases the PTL range to meters, enabling chip-to-chip and board-to-board interconnect.

Fig. 1a shows the design of the LBW data link. All components are AC-powered through inductive transformers. The LBW driver produces 7-10 SFQ pulses per bit, which requires the mutual inductance of the L2 transformer to be about ten times larger than the standard for RQL circuits. The LBW produces bipolar pulses 16 ps wide, FWHM. The LBW is triggered by a bipolar SFQ input and includes a floating buffer junction to prevent back-action on the driving JTL. Circuit dynamics are those of the self-resetting gate first described in [25]. Note that the width of the generated pulse is still low compared to the clock period, giving the latching circuit adequate time to reset and avoiding elevated bit-error-rate associated with Josephson switching errors. The current version of the driver can support up to 10 Gbps throughput per link with 3 fJ/bit dissipation, including a 300 W/W cooling overhead. The receiver achieves a wide timing window of 80° relative to AC clock, while maintaining wide margins of $\pm 30\%$ on AC bias amplitude and about $\pm 50\%$ on individual junction critical current. Spectre simulations of the LBW driver and transmission line, shown in Fig. 1b, use a dispersive propagation model for $1\text{ }\mu\text{m}$ wide Nb $20\text{ }\Omega$ PTL on SiO_2 that accurately models the high frequency components of the pulse, as described in [6].

Different fabrication processes were used for the chips for the two circuit demonstrations. The $5\times 5\text{ mm}^2$ chips were fabricated in the ten-metal-layer SFQ5ee process developed by Lincoln Laboratory [26]. The on-chip resonant clock-power network occupies the bottom two metal layers and is separated from digital logic by a superconducting ground plane. The process features $0.5\text{ }\mu\text{m}$ design rules and Josephson junctions with $10\text{ }\mu\text{A}/\mu\text{m}^2$ critical current density. The $10\times 10\text{ mm}^2$ chips were fabricated in the D-Wave six-metal layer process [27] with a modified junction critical current density of $10\text{ }\mu\text{A}/\mu\text{m}^2$. The process features $0.25\text{ }\mu\text{m}$ design rules for 5 bottom metal layers and $0.5\text{ }\mu\text{m}$ design rules for the top layer. Here the on-chip resonant clock-power network occupies the top two metal layers and is again separated from the digital logic by a superconducting ground plane. In both fabs, the chips are passivated with dielectric and use Ti/Au/Pt pad metallization.

The MCMs for both demonstrations used a well-characterized process for the carrier developed at Lincoln labs [16], and bump bonds also developed at Lincoln. The SMCM4m four-Nb-metal MCM process supports the design of $20\text{ }\Omega$ data PTLs and clock resonator network, with good isolation provided by a superconducting ground plane. The In bump-bond process supports up to 10,000 bumps with $15\text{ }\mu\text{m}$ bump diameter, $35\text{ }\mu\text{m}$ bump pitch, and $3\text{ }\mu\text{m}$ post-bond bump height.

Two kinds of pads were involved in attaching chips to the MCM, shown in Fig. 2. The high frequency,

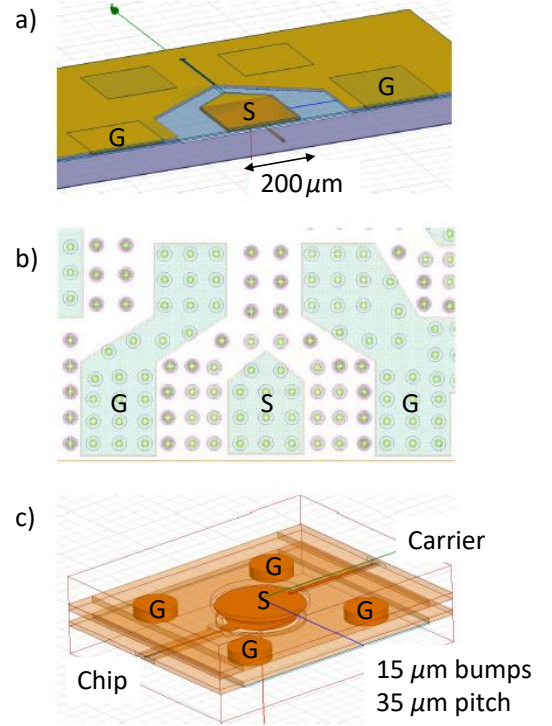


FIG. 2. MCM interconnect. a) Pressure-contact probe packaging of individual chip used a standard pad template with large perimeter pads for clock and data. b) The same pads were used in the MCM attach for clock and I/O signals to room temperature. Multiple bumps were used for signal, ground, and mechanical support. c) High-bandwidth chip-to-chip interconnect used single, $15\text{ }\mu\text{m}$ bumps for each signal and ground pad, on a $35\text{ }\mu\text{m}$ pitch.

$20\text{ }\Omega$ chip-to-chip interconnect used four ground pads surrounding each signal, and had a single bump per pad. This transition was optimized using the HFSS 3D field solver to achieve 350 GHz analog bandwidth with -20 dB reflection. The chip-to-chip clock interconnect used large perimeter pads with multiple bumps. Here the signal integrity requirements are relaxed to a single tone bandwidth between 3.5-10 GHz. The same large perimeter pads are used to mount chips in the standard pressure-contact dip probe and to connect MCM room temperature pads to the chips. This configuration allows test of individual chips prior to mounting in the MCM. In accordance with SMCM4m process design rules, additional non-electrical bump bonds are added along the perimeter for mechanical strength.

Process Control Monitor (PCM) and Time-of-Flight (TOF) resonators are included on the MCM as circuit diagnostics for the MegaZOR and interconnect PTL in order to track fabrication targeting and spread. The PCM structures are characterized with four-port room temperature resistance measurement. These low-cost tests are performed for every MCM on every lot. These data indicate variations in the metal width and thickness. Quarter and half wave TOF resonators are tested at cryo-

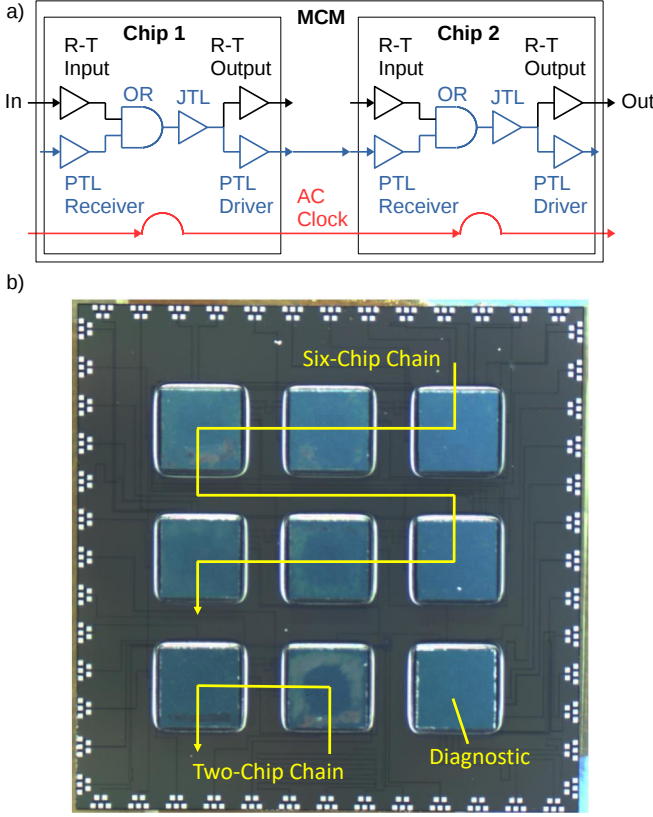


FIG. 3. Synchronous data link with a meander clock. a) Schematic of two interconnected chips. Individual chips can be pre-tested using the room-temperature (R-T) interface prior to populating the MCM. The two-chip chain as shown uses the same R-T interface on the periphery, but uses the PTL interface chip-to-chip. Clock and data take similar paths on the MCM, with similar path lengths. b) Microphotograph of the $32 \times 32 \text{ mm}^2$ MCM populated with nine $5 \times 5 \text{ mm}^2$ chips, showing two-chip and six-chip data links.

genic temperatures using a network analyzer to measure S-parameters. The frequency of the resonance captures variations in the dielectrics and metals. Correlating the PCM and TOF data gives the complete picture of relevant fabrication process parameters.

II. MULTI-CHIP MCM WITH MEANDER CLOCK

The functionality of the on-chip circuitry, and the correctness of the PTL model including transitions between chip and a carrier, was first validated using a nine chip MCM circuit with a meander clock. The meander clock has the advantage of tunable frequency. The meander clock line and signal PTL delay are designed for a 2 GHz clock rate, but as the delays are the same the design works across a large frequency range. The on-chip test circuit has two data paths as shown in Fig. 3a connected to 4 mV output amplifiers for room temperature testing.

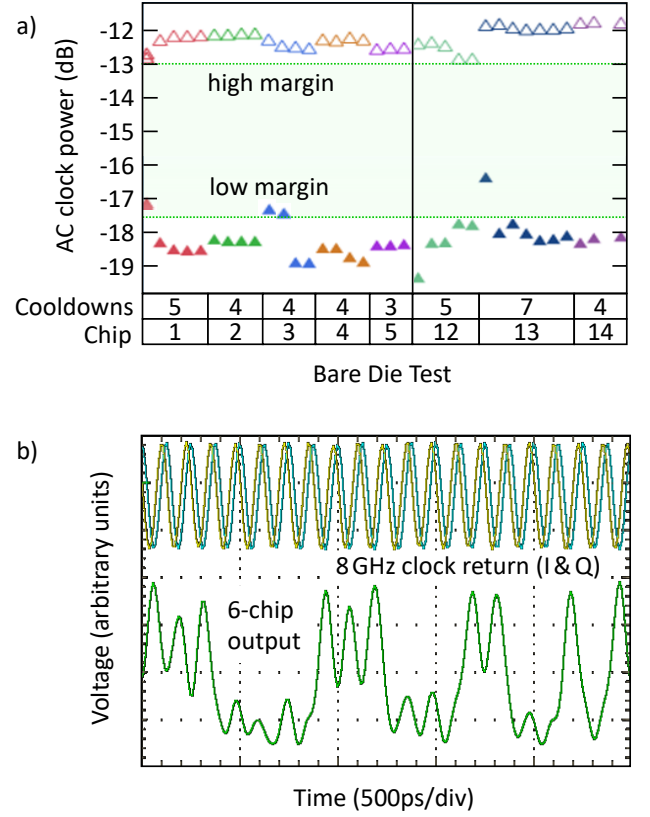


FIG. 4. Meander clock test results. a) Measured AC bias margins for the eight chips tested individually, at 2 GHz and across multiple cooldowns. Typical margins are about 6 dBm. The shaded green region shows a common margin of about 4.5 dB. b) Measured output waveforms through the six-chip chain on MCM at 8 GHz. In data pattern is a repetitive “11110000111000110010” chirp, and the output is averaged.

The first data path is used to pretest individual chips before populating the MCM. The second data path is configured for connection between chips using MCM pads. On-chip circuitry designed in this way also allows to tap into input and output of individual chips on MCM before testing the link through the multiple chips. In this particular MCM design (see Fig. 3b) there are two serial data links going through 6 chips and 2 chips. The last chip was reserved for a different experiment.

Individual chips and the MCM were tested in liquid He dip probes with standard 32-pin and 64-pin pad templates. Tests were performed at-speed with direct connection to room-temperature electronics, using instrumentation and methods similar to that described in [28].

Fifteen individual chips were tested from the same wafer fabricated in the SFQ5ee process, and eight were chosen to populate the chains on the MCM. The individual-chip test for on-chip data paths showed up to 6 dB ($\pm 33\%$) of AC bias margin with common overlap between chips of 4.5 dB, as shown in Fig. 4a. Operating margins across multiple cooldowns showed about 1 dB variation, which is within the design specification

TABLE I. Measured Margins for the Meander-Clock MCM

Build	Frequency	AC Margins
2 Chip Chain	2 GHz	4.3 dB
	8 GHz	3.0 dB
6 Chip Chain	2 GHz	5.4 dB
	8 GHz	3.2 dB

for parasitic coupling to sequestered fluxes in the moats. Similar measurements were taken on the two MCM links with two and six-chip chains, at 2 GHz and 8 GHz clock rate. Output and clock-return waveforms at 8 GHz are shown in Fig. 4b. Both links were functional with measured clock margins as entered in Table I. The operating margins at 2 GHz for both chains are similar to those of the individual chips. Margins at 8 GHz are degraded by about 2 dB, which indicates misalignment of the pulse arrival time within the timing window of the receiver.

III. FOUR-CHIP MCM WITH A RESONANT CLOCK

The demonstration vehicle for synchronous communication using a MegaZOR resonant clock is a $32 \times 32 \text{ mm}^2$ MCM populated with four $10 \times 10 \text{ mm}^2$ chips, shown in Fig. 5. This build represents aggressive scaling due to the large on-chip ZOR clock networks provisioning the entire active area of the $10 \times 10 \text{ mm}^2$ chips. The whole system is capable of powering 4 million Josephson junctions. The increased scale stresses the requirements for resonator amplitude and phase uniformity, bump uniformity, and fabrication parameter spread. On-chip circuitry is similar to that discussed in the previous section, but with an additional synchronous data link providing a loop-back on-chip, in parallel to the chip-to-chip data link. The four chips are connected with two short 5 mm PTLs and a long 54 mm PTL that is one cycle longer at 2 GHz. Allocation of extra taps along the data path enables test of all four chips individually, in pairs and in threes including chip-to-chip communication, and complete test of data propagation through all four chips.

The schematic of the MegaZOR on the MCM is shown in Fig. 6a. It consists of four branches each connected to the individual chip resonator. Each branch consists of two segments with 90° and 270° passive transmission line (PTL) resonators, which positions the connections between circuit segments at voltage anti-nodes. The impedances of the segments are adjusted to achieve a total effective loaded quality factor of resonator of $Q_{\text{load}} = 73$. This represents a nice compromise between minimizing input power and maximizing the bandwidth.

There are two distinct MegaZOR networks for I and Q, electrically identical but with different physical layout. In the current four metal layer MCM process, the resonant network occupies the first metal layer and is sep-

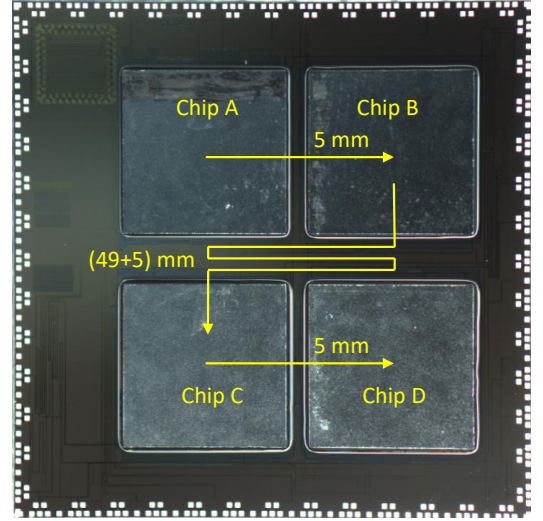


FIG. 5. Microphotograph of the $32 \times 32 \text{ mm}^2$ resonant-clock MCM populated with four $10 \times 10 \text{ mm}^2$ chips, showing short and long signal paths between chips driven by a common resonator.

arated from data transmission lines by a superconducting ground plane in the second metal layer. This constrains the layout to minimize the number of crossovers between the I and Q networks. Physical layout components were simulated using Ansys HFSS to determine impedances and propagation speeds, and sensitivities to process variations. The top-level netlist was simulated using Keysight's Advanced Design System (ADS).

Fig. 6b shows simulated current amplitudes at the spines of the four chips in the worst-case assumption of chip frequency mismatch range of $\pm 0.5\%$ and three different carrier frequencies at nominal, 2 GHz, and $\pm 1.5\%$ from nominal. In the ideal case when there is no mismatch in frequency chip-to-chip and chip-to-MegaZOR, the entire system has a single resonance frequency with near-zero currents at the spines, which are voltage antinodes. The frequency mismatch causes elevated currents in the spines due to shift from ZOR mode towards the first mode and an increase in total drive power. For the worst case described above, our design was optimized to a maximum 50 mA variation of the current in the spines. The parasitic current in the spine divides across multiple ribs of the on-chip resonator. For the current design with about 100 ribs at the current antinode carrying a nominal current of 5 mA, the total resulting variation of the bias current amplitude as seen by the circuit junctions is less than 1% and the input amplitude adjustment to the system is only 1.5 dB.

Two MCMs were built using the two sets of chips, entered in Table II, with resonant frequencies within 0.45% of each other and within $\pm 1\%$ of the MegaZOR frequency of the MCM. Measurement of the on-carrier PCM resonators showed good targeting of the fabrication process, with speed-of-light within 1% of the design value.

Table II also lists the measured AC clock margins for

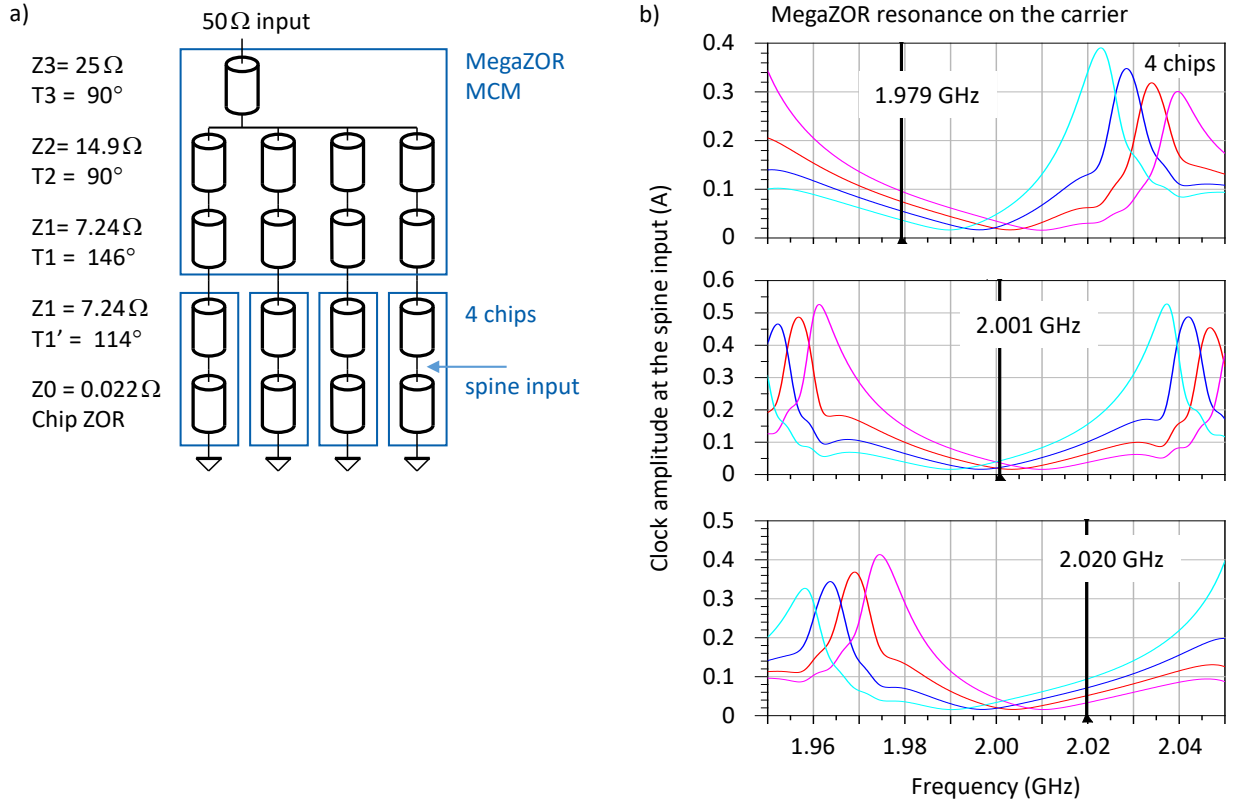


FIG. 6. MegaZOR design. a) Schematic showing four identical branches of transmission line segments, each connected to the ZOR resonator on an individual chip. The segment length is given in degrees at the resonance frequency. b) Simulated current amplitude at the spines of on-chip resonator as function of frequency given for three different cases. The middle panel corresponds to the case with total 1% mismatch between individual chip resonances frequencies with 2 chips being at $\pm 0.5\%$ and 2 chips being at $\pm 0.167\%$ from central frequency of 2 GHz. Maximum spine current amplitude at the drive frequency is 42 mA. The top and bottom channels correspond to the cases with added carrier MegaZOR frequency variation of $\pm 1.5\%$ on top of the frequency distribution between chips. Maximum spine current amplitude at the drive frequency is 50 mA.

TABLE II. Measured Margins for Individual Chips and for Chip Chains on the MCM with a Resonant Clock

Build	Test Path	Resonance	AC Margins
1	Chip A	1.973 GHz	2.5 dB
	Chip B	1.974 GHz	4.5 dB
	Chip C	1.982 GHz	5.0 dB
	Chip D	1.976 GHz	3.0 dB
	MCM Chips A-B		untestable*
	MCM Chips C-D		4.8 dB
	MCM Chips A-B-C		untestable*
2	Chip A	2.019 GHz	4.0 dB
	Chip B	2.011 GHz	4.0 dB
	Chip C	2.019 GHz	3.5 dB
	Chip D	2.031 GHz	4.5 dB
	MCM Chips A-B		2.0 dB
	MCM Chips C-D		2.5 dB
	MCM Chips A-B-C		1.0 dB

*Untestable due to signal continuity failures on MCM

the pretested chips and for the synchronous data links between chips. Only the short path between chips C and D was testable on Build 1 due to signal continuity failures. Measured margins for this path are on par with those of the individual chips, indicating no degradation due to the MCM transition. The applied clock frequency was tuned to the mean resonance of Chips C and D for this test. Build 2 shows functionality of all links between the four chips. The operating margin for the links varied from 2.5 dB for the short links to 1 dB to the longest link through Chips A, B, and C.

Simulation in ADS and HFSS, based on back-annotation of the carrier physical layout, showed that the margin degradation is due to inconsistent design of crossovers between I and Q carrier resonators resulting in an imbalance between the four branches of MegaZOR. As the imbalance between the two chips tested in Build 1 is small, the effect on margins is minimal. We conclude that the margin degradation could be corrected in a re-design, and that synchronous communication at the scale for four $10 \times 10 \text{ mm}^2$ chips is practical.

IV. CONCLUSION

In this paper we have presented design and test results for synchronous communication links between multiple chips on an MCM using resonant clock distribution. These results advance state-of-the-art in superconducting digital technology in multiple ways. It is the first demonstration of superconducting data links on MCM involving multiple chips. The system demonstrates the power of synchronous communication in RQL technology overcoming the difficulties of clock recovery and accumulated thermal jitter and parametric timing uncertainty associated with RSFQ technology. We have shown that digital data on MCM can be transmitted across 54 mm between chips with minimal hardware overhead as the LBW driver and receiver have only six Josephson junctions, dissipating only 3 fJ taking the 300 W/W cooling overhead into account. The energy transmitted per bit is three orders of magnitude less than state-of-the-art CMOS BoW-style data links for the same purpose and distance. The 2 GHz clock frequency in the current

demonstration can be scaled up to 10 GHz based on circuit simulation of the LBW driver, limited by dispersion of the Nb interconnects. Extension to multi-bit bus communication is straight forward, with total cross-sectional bandwidth between chips limited only by bump pitch. All told, we have enabled a critical interconnect functionality for future RQL systems distributed on multiple chips using 3D-IC advanced packaging.

ACKNOWLEDGMENTS

The authors acknowledge Andrew Brownfield for developing high frequency test setup and assisting with circuit test, and Paul Chang for assisting with data reduction and analysis. Authors also acknowledge the contributions of the Lincoln Laboratory team, particularly Rabindra Das and Sergey Tolpygo, in numerous technical discussions regarding the MCM carrier and bonding process, and assistance with design. The Northrop Grumman superconducting digital EDA and PDK teams laid the foundation for MCM design and verification.

-
- [1] D. A. Miller, *Journal of Lightwave Technology* **35**, 346 (2017).
 - [2] S. Polonsky, V. Semenov, and D. Schneider, *IEEE Transactions on Applied Superconductivity* **3**, 2598 (1993).
 - [3] M. Tanaka, T. Kondo, N. Nakajima, T. Kawamoto, Y. Yamanashi, Y. Kamiya, A. Akimoto, A. Fujimaki, H. Hayakawa, N. Yoshikawa, et al., *IEEE transactions on applied superconductivity* **15**, 400 (2005).
 - [4] M. Rafique, I. Kataeva, H. Engseth, M. Tarasov, and A. Kidiyarova-Shevchenko, *Superconductor Science and Technology* **18**, 1065 (2005).
 - [5] A. Shukla, B. Chonigman, A. Sahu, D. Kirichenko, A. Inamdhar, and D. Gupta, *IEEE Transactions on Applied Superconductivity* **29**, 1 (2019).
 - [6] V. V. Talanov, D. Kneé, D. Harms, K. Perkins, A. Urbanas, J. Egan, Q. Herr, and A. Herr, *arXiv preprint arXiv:2104.07371* (2021).
 - [7] Q. P. Herr, M. S. Wire, and A. D. Smith, *IEEE transactions on applied superconductivity* **13**, 463 (2003).
 - [8] Y. S. Shao, J. Clemons, R. Venkatesan, B. Zimmer, M. Fojtik, N. Jiang, B. Keller, A. Klinefelter, N. Pinckney, P. Raina, et al., in *Proceedings of the 52nd Annual IEEE/ACM International Symposium on Microarchitecture* (2019), pp. 14–27.
 - [9] R. Farjadrad, M. Kuemerle, and B. Vinnakota, *IEEE Micro* **40**, 15 (2019).
 - [10] D. S. Holmes, A. L. Ripple, and M. A. Manheimer, *IEEE Transactions on Applied Superconductivity* **23**, 1701610 (2013).
 - [11] Q. P. Herr, A. Y. Herr, O. T. Oberg, and A. G. Ioannidis, *Journal of Applied Physics* **109**, 103903 (2011).
 - [12] A. F. Kirichenko, I. V. Vernik, J. A. Vivalda, R. T. Hunt, and D. T. Yohannes, *IEEE Transactions on Applied Superconductivity* **25**, 1 (2014).
 - [13] A. Y. Herr, Q. P. Herr, O. T. Oberg, O. Naaman, J. X. Przybysz, P. Borodulin, and S. B. Shauck, *Journal of Applied Physics* **113**, 033911 (2013).
 - [14] T. Filippov, D. Amparo, M. Kamkar, J. Walter, A. Kirichenko, O. Mukhanov, and I. Vernik, in *2017 16th International Superconductive Electronics Conference (ISEC)* (IEEE, 2017), pp. 1–4.
 - [15] F. China, N. Tsuji, T. Narama, N. Takeuchi, T. Ortlepp, Y. Yamanashi, and N. Yoshikawa, *IEEE Transactions on Applied Superconductivity* **27**, 1 (2016).
 - [16] R. N. Das, V. Bolkhovsky, S. K. Tolpygo, P. Gouker, L. M. Johnson, E. A. Dauler, and M. A. Gouker, in *2017 IEEE 67th Electronic Components and Technology Conference (ECTC)* (2017), pp. 675–683.
 - [17] S. B. Kaplan, V. Dotsenko, and D. Tolpygo, *IEEE transactions on applied superconductivity* **17**, 971 (2007).
 - [18] Y. Hashimoto, S. Yoroze, T. Satoh, and T. Miyazaki, *Applied Physics Letters* **87**, 022502 (2005).
 - [19] S. Narayana, V. Semenov, Y. Polyakov, V. Dotsenko, and S. Tolpygo, *Superconductor Science and Technology* **25**, 105012 (2012).
 - [20] R. Kashima, I. Nagaoka, M. Tanaka, T. Yamashita, and A. Fujimaki, *IEEE Transactions on Applied Superconductivity* **31**, 1 (2021).
 - [21] M. E. Çelik, T. V. Filippov, A. Sahu, D. E. Kirichenko, S. M. Sarwana, A. E. Lehmann, and D. Gupta, *IEEE Transactions on Applied Superconductivity* **30**, 1 (2020).
 - [22] J. Strong and et. al., to be published (2021).
 - [23] H. Dai and et. al., to be published (2021).
 - [24] R. L. Kautz, *Journal of Applied Physics* **49**, 308 (1978).
 - [25] H. Chan, W. Lum, and T. Duzer, *IEEE Transactions on Magnetics* **11**, 770 (1975).
 - [26] S. K. Tolpygo, V. Bolkhovsky, R. Rastogi, S. Zarr, A. L. Day, E. Golden, T. J. Weir, A. Wynn, and L. M. Johnson, *IEEE Transactions on Applied Superconductivity* **29**, 1

- (2019).
- [27] A. Berkley, M. Johnson, P. Bunyk, R. Harris, J. Johansson, T. Lanting, E. Ladizinsky, E. Tolkacheva, M. Amin, and G. Rose, *Superconductor Science and Technology* **23**, 105014 (2010).
- [28] J. Egan, A. Brownfield, and Q. Herr, arXiv preprint arXiv:2104.07372 (2021).